Nuclear Science and Techniques (2025) 36:101
https://doi.org/10.1007/s41365-025-01687-3

Concept design of an X-ray probe tube for deep-sea mineral exploration

Lang Dong[1] · Ming Wang[1] · Qing-Xian Zhang[1,2] · Hong-Fei Xiao[1] · Biao Jiang[1] · Zi-Yang Wang[1] · Chun-Hui Dong[1,2] · Yi Gu[1,2]

Received: 6 April 2024 / Revised: 19 June 2024 / Accepted: 1 July 2024 / Published online: 19 April 2025
© The Author(s), under exclusive licence to China Science Publishing & Media Ltd. (Science Press), Shanghai Institute of Applied Physics, the Chinese Academy of Sciences, Chinese Nuclear Society 2025

Abstract

Promoting the development of deep-sea mineral exploration instrumentation can help alleviate the global resource shortage faced by mankind. X-ray fluorescence (XRF) spectrometry has been widely used in the in situ analysis of deep-sea minerals owing to its fast analytical speed, nondestructive nature, and wide analytical range. This study focused on the structural safety and detection efficiency of X-ray fluorescence in situ measurement equipment under high pressure for deep-sea XRF analysis. This study first combined finite element analysis and experiments to design and optimize the structure of an X-ray probe tube required for deep-sea mineral exploration and to determine the Be window thickness to ensure stress safety. Subsequently, the Monte Carlo method was used to analyze and optimize the Be window thickness on the X-ray probe tube to improve the accuracy of the elemental analyses. Finally, the effect of seawater thickness between the transmitter outer tube and rock wall was also considered. The results show that based on ocean depth in different detection environments, Be windows with a thickness of 1.5 mm or 2.0 mm can be selected to improve the detection efficiency of the device while ensuring the structural safety of the instrument. According to the design features and detection requirements of the device, in deep-sea exploration of minerals with characteristic peak energies below 10 keV, the transmitter outer tube should be as close as possible to the rock wall inside the logging. When the characteristic peak energy of the minerals is more than 10 keV, the distance between the transmitter outer tube and rock wall inside the logging should be controlled to approximately 2 mm. This study provides feasible solutions for future deep-sea mineral resource development and a useful reference for elemental analysis of minerals in the deep-sea or other extreme working environments.

Keywords X-ray probe tube · Be window · Structure design · Detection efficiency

1 Introduction

With the industrial development in recent years, mineral reserves on land have gradually been reduced or even depleted [1–3]. However, there are abundant mineral resources in the deep oceans, and accelerating the exploration and exploitation of deep-sea minerals will aid in alleviating current resource constraints [4–6]. However, deep-sea mineral exploration is an emerging area, and standard laws and regulated exploration methods are yet to be perfected [6–8]. Therefore, it is important to design an exploration device capable of continuously measuring and analyzing the mineral composition of the deep-sea. This will facilitate the effective exploitation of deep-sea mineral resources.

Currently, deep-sea mineral exploration relies primarily on equipment such as deep-sea mining vehicles or manned

This work was supported by the National Major Scientific Research Instrument Development Projects (No. 42127807) and the National Natural Science Foundation of China (No. 12105030).

✉ Ming Wang
wangming1@cdut.edu.cn

[1] College of Nuclear Technology and Automation Engineering, Chengdu University of Technology, Chengdu 610059, China

[2] Applied Nuclear Technology in Geosciences Key Laboratory of Sichuan Province, Chengdu University of Technology, Chengdu 610059, China

submersibles that transport the collected samples to land or ships for elemental analysis (using X-ray fluorescence spectrometry (XRF) and other methods) [9–11]. However, the complexity and variability of deep-sea geomorphological environments prevent many of these devices from accurately and efficiently collecting mineral samples. This leads to certain limitations in these methods for deep-sea mineral exploration. Simultaneously, if deep-sea mineral mining is performed blindly without precisely locating mineral deposits, it will cause irreversible damage to fragile marine ecosystems [12, 13]. In contrast, land-based mineral exploration relies primarily on traditional drilling platforms for sampling and analysis. For example, Peng et al. conducted a mineral analysis study of uranium deposits in the Erlian Basin of Inner Mongolia based on XRF and proposed ground leaching mining of sandstone-type uranium ores from the perspective of time-delayed mineralogy [14]. Based on the SRXRF and INAA methods, Kolmogorov et al. developed a method that can analyze rock ores with complex compositions and developed a method that can be used to detect platinum group elements [15]. If accurate exploration of deep-sea mineral distributions is combined with land-based logging techniques, deep-sea mining would have a significant advantage over traditional land-based mining [16–18].

According to related literature, veins such as sulfide ore or manganese nodules (MNs) in the ocean generally occur at depths of 3000 m–6000 m or near deep-sea volcanic mountains [19, 20]. However, the extreme high temperature and high pressure environments in the region pose a significant challenge to deep-sea exploration. In this context, conducting efficient and environmentally friendly mineral exploration is an important issue that needs to be addressed. Therefore, to a practicable extent, adverse environmental impacts should be reduced using advanced equipment or improve mining methods. This may involve ensuring that the exploration equipment is structurally adapted to extreme environments, minimizing the interaction between the exploration appliances and the environment, or adopting vertical slit-fill exploration and collection [21–23]. It is important to optimize the above aspects for the analysis of mineral element results.

The purpose of this study is to solve the problem of existing X-ray detection equipment in the deep-sea or other extreme working conditions, owing to extreme pressure differences or temperature factors causing safety accidents and detection difficulties, and to conduct an early laboratory structural prototype development of a deep-sea X-ray probe tube required for mineral exploration in the Indian Ocean. First, this study focuses on the mechanical structure design of the area containing the X-ray transmitting and receiving system using finite element analysis to analyze the stresses and displacements of the mechanical structure in detail. The actual test method was also used to verify the stability of the model. Second, the Monte Carlo method was used to analyze the effect of the Be window thickness on the X-ray transmittance of the X-ray probe tube in detail. Finally, the effect of seawater thickness between the X-ray probe tube and the well wall formation on logging detection efficiency is discussed. The experimental study of this device can serve as a reference for the *in situ* characterization and analysis of minerals in the deep-sea or other extreme working environments.

2 Materials and methods

2.1 Deep-sea mineral X-ray survey device design

The overall structure of the X-ray probe tube comprises mainly four systems. A simplified diagram of its structure and a schematic of its working mode are shown in Fig. 1. Each system and its main components are respectively referred to as follows:

1. Outer shell system: Drill pipe joints, drill pipes, etc.
2. Sealing system: Supporting sealing seat, sealing needle seat, and sealing head, etc.
3. X-ray transmitting and receiving system (core system): Transmitter outer tube, compression spring, Be window, X-ray source, silicon drift detector (SDD), etc.
4. Electronic systems: Nuclear signal data processing devices, high-temperature-resistant battery power supply devices, spring expansion control devices, data storage devices, USB boards, etc.

To ensure minimal structural deformation and displacement of the X-ray survey device at a depth of approximately 4000 m, the entire device was designed as a cylinder (the pressure on an object in water is directly proportional to its surface area in contact with water, and the surface area of a cylindrical structure is smaller for the same volume). The internal pressure of the X-ray transmitting and receiving system should be maintained at standard atmospheric pressure to protect the core equipment, such as the X-ray source and SDD, from damage. Referring to the titanium alloy material used in the Chinese manned submersible Jiaolong, which completed the 7000 m sea trial in 2012 [24, 25], the Ti-6Al-4V (annealed) titanium alloy with a maximum ultimate compressive strength of 2042 MPa was selected as the housing material for the X-ray probe tube [26].

According to the design requirements, the outer tube of the transmitter was initially designed as a hollow cylinder with an inner diameter of 62 mm and an outer diameter of 72 mm. The X-ray exit aperture has a 3 mm arc radius at both ends and 9 mm length in the center. The X-ray reflection aperture has a radius of 5 mm Exploration is conducted in the deep-sea mainly for veins such as MN

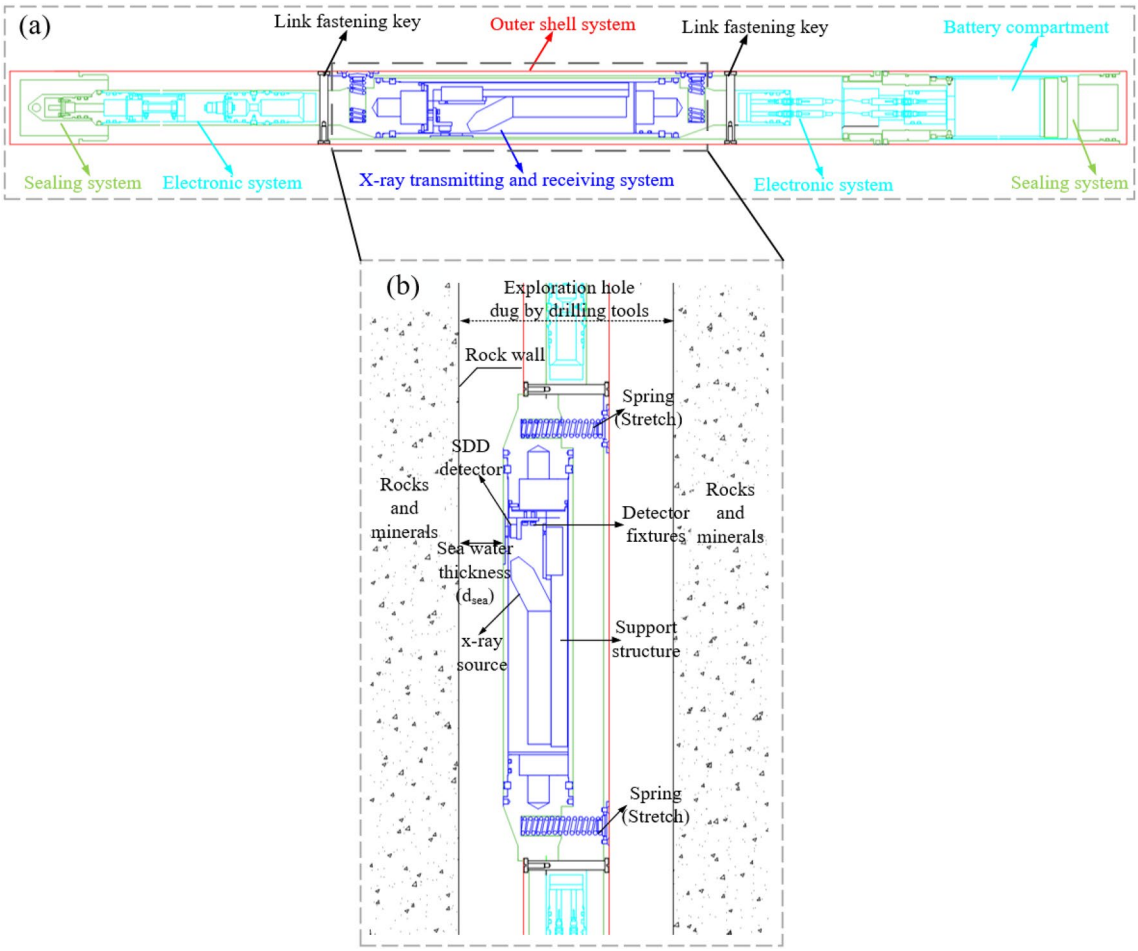

Fig. 1 (Color online) Schematic of the X-ray tube. **a** Overall structural design of the device schematic; **b** working diagram of the device

ores or cobalt ores. To accurately identify the constituent elements of deep-sea minerals, the X-ray probe tube must be capable of detecting characteristic X-rays with energies ranging from 1 keV to 20 keV. The device was designed to use an X-ray tube with Ag as the anode target and X-ray source.

Seawater causes additional scattering and energy attenuation of X-rays from the target elements, which complicates the energy spectrum received by the detector. Therefore, the X-ray exit and reflection apertures of the device must be coated with Be windows of a certain thickness to remove the influence of low-energy X-rays. However, there is a difference in hardness between Be and Ti-6Al-4V. Moreover, the thickness of the Be layer directly affects the final detection efficiency of SDD. Consequently, the Be window thickness should also be analyzed in detail to determine the optimal thickness for improving the efficiency and safety of the equipment.

2.2 FEA model

The X-ray detection system was originally designed to use a compression spring to push the outer tube of the transmitter containing the X-ray source and SDD out of the housing at a certain distance. This design facilitated the collection and analysis of the mineral constituents (for the working principle, refer to Fig. 1(b)). To simplify the computational complexity, the X-ray transmission and reception systems can be analyzed as separate structures. At the same time, to maximize the assessment of the structural safety of the system, critical structures such as the support seal seat, Be window, and internal support frame will be retained during the experiments.

When plating Be on the X-ray exit and reflection holes of the outer tube of the transmitter, it is necessary to remove an equal amount of Ti-6Al-4V from the surface of the shell according to the thickness of the Be window.

Therefore, the 3D model of the Be window is designed as a cube with a changeable thickness and certain curvature according to experimental needs. Simultaneously, the area where the Be window is located in the outer tube of the transmitter is dug and patched to ensure that the surface of the Be window is parallel to the outer surface of the transmitter's outer tube. This was done to minimize the possibility of damage to the X-ray probe tube due to collision of the Be window with the external environment during submersion or operation. The final 3D structural device diagram used for the safety assessment analysis is shown in Fig. 2. This experiment investigated the stress analysis of Be windows with different thicknesses in extreme environments, and thus, the Be window thicknesses (d_{Be}) were designed as 1.0 mm, 1.5 mm, 2.0 mm, 2.5 mm, and 3.0 mm for structural simulation experiments.

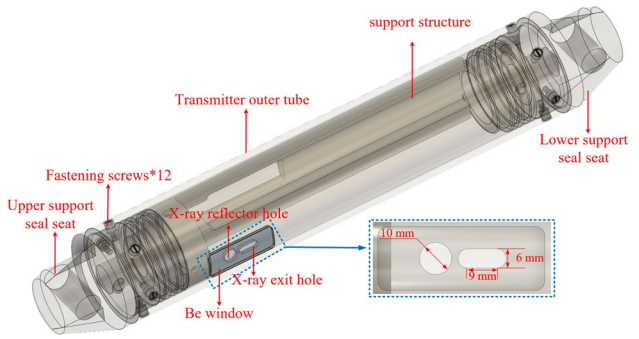

Fig. 2 (Color online) 3D structural model of the X-ray transmitting and receiving system

The ANSYS Workbench mesh tool was used to generate the mesh during finite element analysis of the model. A tetrahedral mesh of size 4 mm was utilized for finite element discretization calculations. Because the Be window, X-ray exit, and reflection holes are critical structures that need to be analyzed for structural safety, the mesh in this area should be encrypted. The encryption method was based on an arc with a radius of 16 mm centered at the midpoint of the Be window, where the encrypted mesh was 0.4 mm, resulting in an approximately 1.42 million meshes for calculation.

Because the device can be used near a submarine volcanic mountain range, the environmental temperature during the simulation was set to 373.15 K. The end face of the upper support sealing seat is designated as a fixed support surface, and the hydrostatic pressure needs to be considered when calculating the surface effect, where the density of water is approximately $1 \times 10^3 \mathrm{kg/m^3}$ and gravitational acceleration is $9.8 \mathrm{m/s^2}$, the system was simulated in liquid water at depths of 1,000, 2,000, 3,000, and 4,000 m. The model used for the structural safety analysis is shown in Fig. 3. The material of the fastening screws was 304 stainless steel, and the transmitter outer tube was Ti-6Al-4V (annealed). The engineering data of the relevant materials used for the pressure simulation are shown in Table 1.

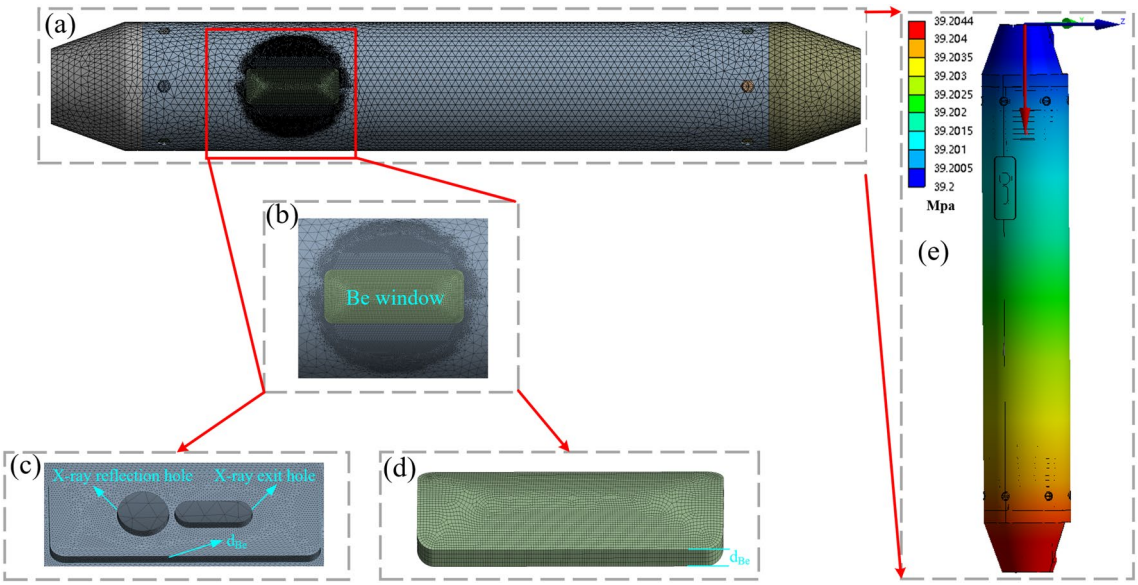

Fig. 3 (Color online) X-ray transmitting and receiving system mesh model and detail. **a** Transmitter outer tube, Be window, upper and lower support seats mesh model. **b** Encrypted mesh in the Be window region. **c** Encrypted mesh at the X-ray exit and reflection holes. **d** Mesh model of the Be window. **e** Initial state stress distribution at seawater depth 4000 m

Table 1 Related materials engineering data sheet

	Be	Ti-6Al-4V (annealed)	304 stainless steel
Density (kg/m^3)	1848	4429	7750
Young's modulus (Pa)	3.0×10^{11}	1.112×10^{11}	1.93×10^{11}
Poisson's ratio	0.07	0.3387	0.31
Thermal expansion coefficient (C^{-1})	1.206×10^{-5}	8.789×10^{-6}	1.7×10^{-5}
Tensile yield strength (Pa)	2.3994×10^{8}	8.457×10^{8}	2.07×10^{8}
Tensile ultimate strength (Pa)	3.7025×10^{8}	9.18×10^{8}	5.86×10^{8}

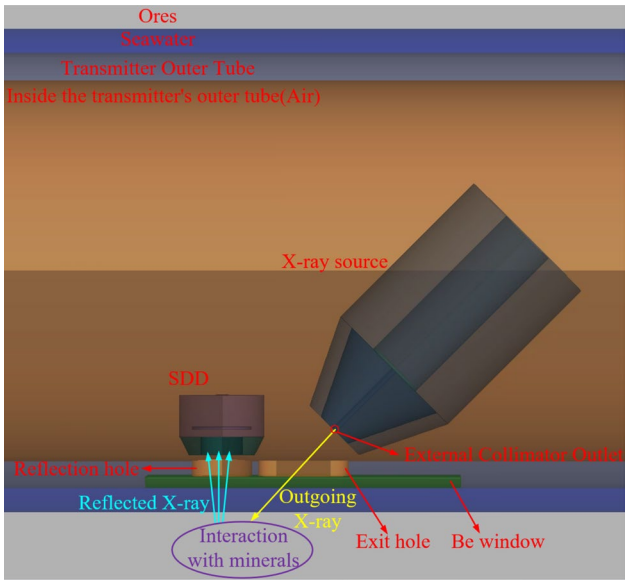

Fig. 4 (Color online) Monte Carlo simulation (partial) of the X-ray transmitting and receiving system

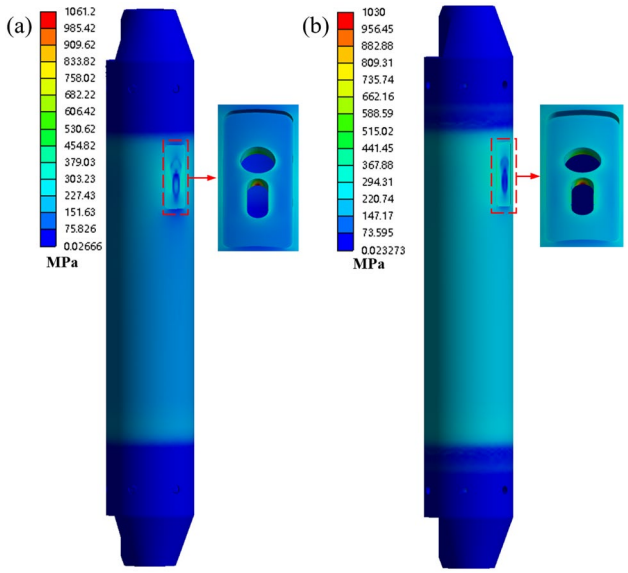

Fig. 5 (Color online) FEA results of the transmitter outer tube. **a** von-Mises stress distribution contour map for d_{Be} = 1.5 mm (seawater depth 3000 m); **b** von-Mises stress distribution contour map for d_{Be} = 2.0 mm (seawater depth 4000 m)

2.3 Monte Carlo model

The Monte Carlo simulation experiments were performed using Geant4−11.1.2, and the simulation model is shown in Fig. 4. The Ag target was 0.005 mm thick, the radius was 5 mm, the Be window thickness was 0.5 mm, the inner collimator inside the diameter of The X-ray tube was 5 mm, and the outer collimator inner diameter was 0.5 mm. SDD used VITUS H20 manufactured by KETEK (in the actual equipment, semiconductor thermoelectric cooling technology was used. The operating environment of the probe assembly was maintained at 238.15 Kusing a secondary cooling component). The ambient temperature in the experiment was set to 373.15 K and the pressure was set to 400 atm. To improve the accuracy of the experiment in the simulation, initially 5×10^9 electrons with an energy of 50 keV were emitted to bombard the Ag target of the X-ray tube. The X-ray energy spectrum at the exit of the external collimator was recorded and analyzed. Subsequent experiments used this spectrum to replace the particle source generated by the X-ray source unit during operation.

3 Results and discussion

3.1 Structural safety analysis

From the FEA results, the stress and displacement magnitude distributions were similar for different Be window thicknesses. Figure 5 shows the simulated von-Mises stress contour maps of the transmitter outer tube, X-ray exit hole, and reflection hole at seawater depths of 3000 m and 4000 m for d_{Be}=1.5 mm and 2.0 mm. The results show that the von-Mises stress zone on the device is mainly located at the junction of the X-ray exit and reflection holes. In contrast, the stresses on the surface of the transmitter's outer tube were concentrated in the middle region of the outer tube because the ends of the outer tube of the transmitter contained sealing seat fillers to withstand the stresses (Fig. 2). The results show that the middle portion

of the outer tube of the transmitter is subjected to higher von-Mises stresses than that at the ends.

Concerning the Be window plating on the outer tube of the transmitter, because the Be window's interior is in direct contact with the edges of the X-ray exit and reflection holes, this may result in an outlier in the pressure in a specific area inside the Be window. Therefore, the stress distribution and displacement of the Be window must be analyzed separately. Based on Fig. 5, the Be window was calculated separately, and the results are shown in Fig. 6. The results show that under seawater pressure, an extreme stress distribution similar to the hole shape occurred on the internal face of the Be window. This is because in the original design, there was no material blocking the two holes to minimize the interaction of X-rays with other objects during motion, which reduces the contact area in the center area of the Be window, resulting in extreme stresses. However, the entire Be window is embedded in the outer tube of the emitter and the Be window edge area coincides with the outer tube of the emitter. This better transfers the pressure exerted on the edge of the Be window to the outer tube of the emitter.

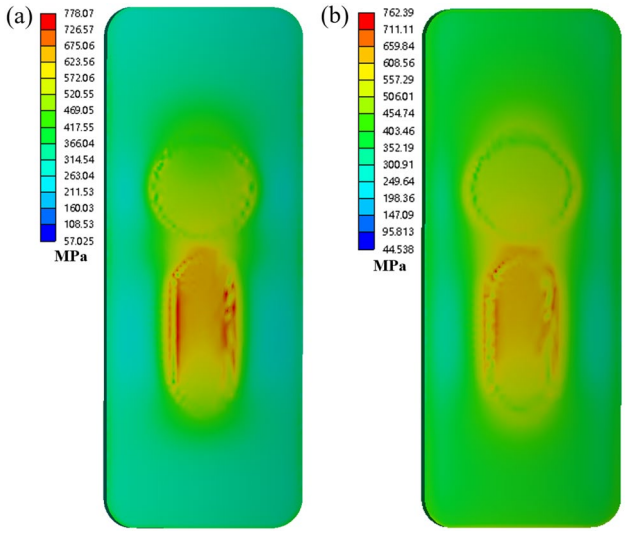

Fig. 6 (Color online) FEA results of the Be window. **a** von-Mises stress distribution contour map for d_{Be} = 1.5 mm (seawater depth 3000 m); **b** von-Mises stress distribution contour map for d_{Be} = 2.0 mm von-Mises stress distribution contour map for d_{Be} = 2.0 mm (seawater depth 4000 m)

From the results shown in Figs. 5 and 6, the X-ray exit hole and reflection hole regions generate higher von Mises stresses near this region than in other regions of the transmitter outer tube, which may cause breakage of the transmitter outer tube structure or the Be window, ultimately affecting X-ray transmission. Because the Be window is not only designed to block seawater from entering the tube but also to be as thin as possible under structural safety conditions (the Be window thickness has a significant effect on X-ray attenuation), the Be window's optimal thickness must be determined through rigorous calculations. Fig. 7 shows the trend plot of the maximum stress between the Be window and two holes of the transmitter outer tube for different Be window thicknesses under different deep-sea pressures. The results in Fig. 7(a) show that the magnitudes of the stresses on both decreased as the Be window thickness increased. Be is easily oxidized in air to form BeO (its maximum compressive strength is approximately 1551 MPa [27]). To ensure structural safety of the entire system, Be window detectors with corresponding thicknesses within the safe stress threshold can be selected for measurements based on the seawater depth of the actual measurement environment.

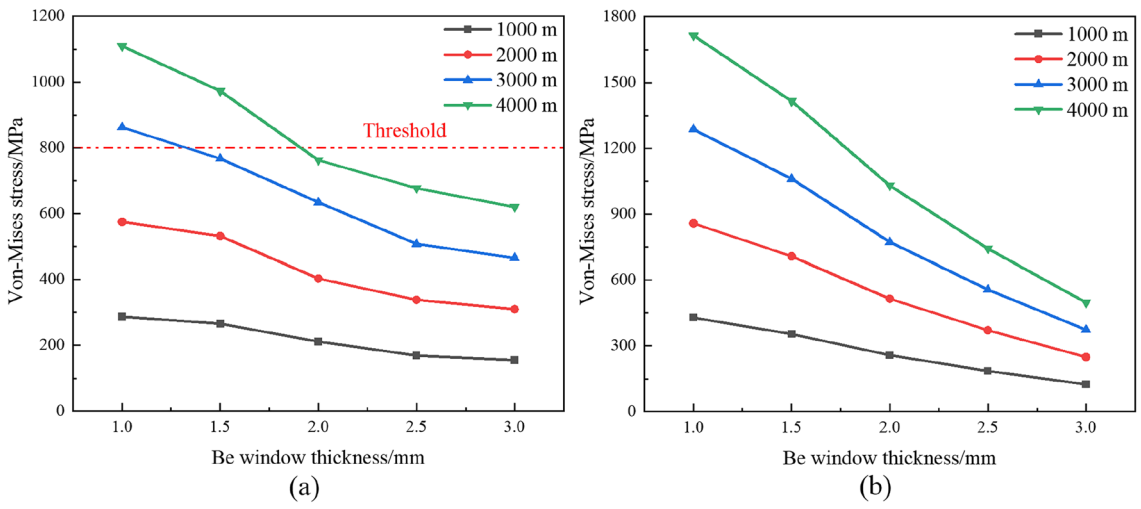

Fig. 7 (Color online) Trend of the von-Mises stress for systems having Be windows of different thicknesses at different seawater depths. **a** Trend of von-Mises stress for the Be window. **b** Trend of von-Mises stress between two holes on the transmitter outer tube

Based on the results of the above FEA, two preliminary deep-sea mineral exploration X-ray detectors (with Be-window thicknesses of 1.5 mm and 2.0 mm) were produced for this experimental test. The Be window was bonded to the designated area of the outer transmitter tube using LEAFTOP casting adhesive, which has an operating temperature between 218.15 K and 493.15 K and is highly waterproof and rigid. The two devices were shipped to Changsha Institute of Mining Research Co., Ltd., Hunan Province, China, for high-pressure damage testing (Fig. 8). The test procedure involved placing the device in well pressurizers, while gradually increasing the pressure in the well by following a process from 0 MPa to 40 MPa. The results show that no anomalies were produced in the structure of the two devices under the experimental conditions at pressures ranging from 0 MPa to 40 MPa, and the surface of the Be window did not show any significant breakage. However, combined with the FEA results (Figs. 6 and 7), the maximum von-Misese stress exceeded the safety threshold when the Be window thickness was 1.5 mm. Therefore, to avoid device anomalies in future deep-sea exploration, a Be window with a thickness of 1.5 mm can be selected when the ocean depth of the exploration reaches 3000 m, and a Be window with a thickness of 2.0 mm can be selected when the depth of the exploration reaches 4000 m. A Be window with a thickness of 2.0 mm was selected when the exploration depth reached 4000 m.

The initial design and simulation of the entire X-ray probe tube were performed in an extreme working environment. However, during the actual measurement, the device was in the standby mode most of the time to save power, and the temperature of the working environment was maintained at 293.15 K – 313.15 K, which means that the temperature change had no obvious effect on the performance of the device [28, 29], and the effect of ambient temperature on the fatigue of the X-ray probe in the device was negligible at this stage.

3.2 Effect of Be window thickness on X-ray detection efficiency

Be windows have a filtering effect on X-rays in the low-energy range and can effectively filter low-energy bremsstrahlung and scattered X-rays [30, 31]. In general, the Be window should be as thin as possible to increase the X-ray transmission and optimize the instrument performance [32]. To obtain detailed X-ray spectral data, the Geant4 software was first used to calculate the X-ray source's outgoing energy spectrum at the time of operation (the X-ray source and SDD are located 0.1-mm inside the transmitter outer tube wall). Figure 9 shows the X-ray energy spectrum (normalized using the ratio of the statistical photon number to the incident electron number) at the external collimator exit (the geometric structure is shown in Fig. 4).

According to the conclusions drawn from Fig. 7, to ensure that the thickness of the Be window on the transmitter outer tube is as thin as possible under safe working conditions, it is necessary to perform simulation tests for Be window thickness (d_{Be}) at 1 mm, 1.5 mm, 2.0 mm, 2.5 mm, and 3.00 mm. Based on the literature on the properties of ore distribution in the ocean, the ore materials were selected as MnO, FeO, $Co(OH)_2$, and $SrSO_4$ for the experiments [33, 34]. By comparing the characteristic X-ray transmittances of the target elements, Mn, Fe, Co, and Sr, for different Be window thicknesses in these materials (using the X-ray spectra shown in Fig. 9 as a radiation source), it is possible to determine the minimum Be window thicknesses that satisfy safe structural

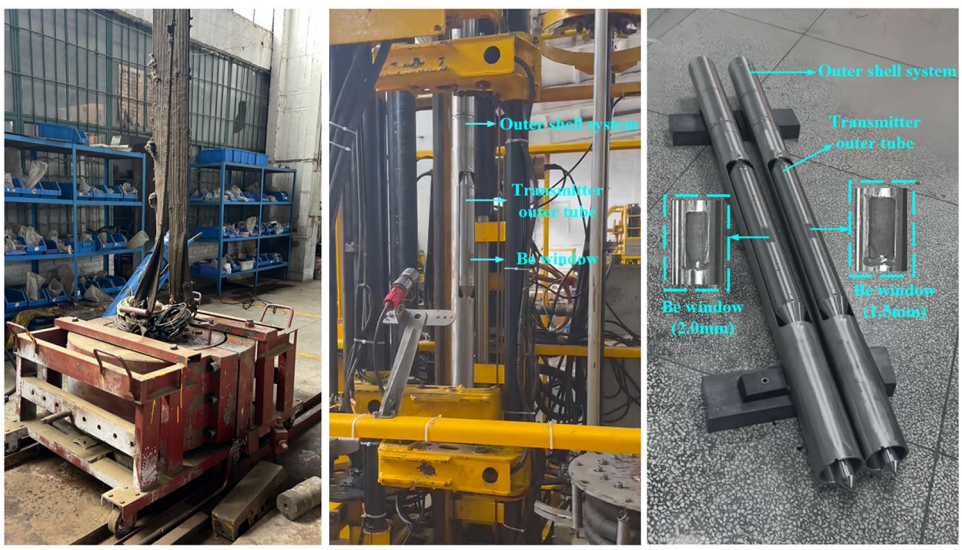

Fig. 8 (Color online) X-ray detector high-pressure damage test chart. **a** Well pressurizers. **b** X-ray detector was being prepared for high-voltage damage testing. **c** X-ray detector and Be window in two sizes after high-pressure damage testing

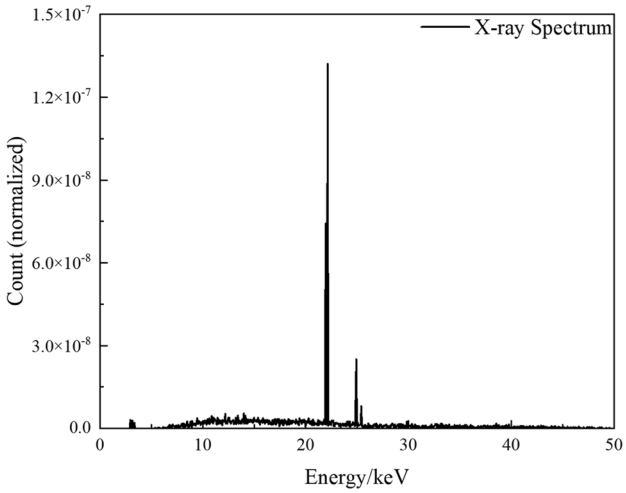

Fig. 9 (Color online) X-ray source's outgoing energy spectrum simulation map

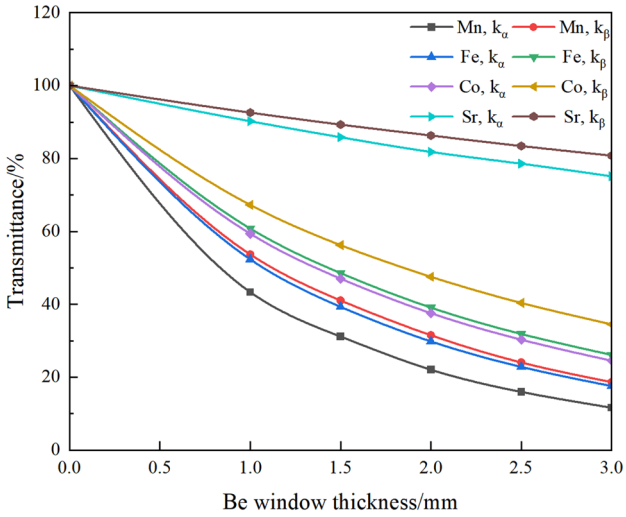

Fig. 10 (Color online) X-ray transmittance for different Be window thicknesses

conditions. The results are presented in Fig. 10, where the X-ray transmittance decreases as the Be window thickness increases. Combined with the structural safety analysis and actual testing of the outer tube of the transmitter and Be window, as shown in Figs. 7 and 8, selecting a Be window with a thickness of 1.5 mm or 2.0 mm can improve the X-ray detection efficiency while ensuring structural safety.

3.3 Effect of seawater thickness on detection efficiency

In addition, it is crucial to determine the distance between the outer tube of the transmitter and rock wall inside the log. This is because it effectively solves the problem of X-ray energy attenuation at different seawater thicknesses (d_{sea}) (see Fig. 1), which is important for the subsequent improvement of SDD detection efficiency [35]. Seawater primarily comprises water and dissolved salts, typically at a concentration of 3.5% [36]; however, dissolved salts produce ions that have no significant effect on the X-ray absorption [37, 38]. Thus, for the simulation analysis of detection efficiency, seawater can be considered as ordinary H_2O.

To investigate the effect of the distance (d_{sea}) between the rock wall inside the logging and Be window on the transmitter outer tube on the SDD detection efficiency, we simulated the energy spectrum statistics of the X-rays received by the SDD for different seawater layer thicknesses (the Be window on the transmitter outer tube was maintained at a thickness of 2 mm during the simulation). A total of 12 cases with seawater thicknesses of 0 mm, 0.5 mm, 1 mm, 2 mm, 3 mm, 4 mm, 5 mm, 6 mm, 7 mm, 8 mm, 9 mm, and 10 mm were analyzed. To control the experimental variables, the experiment used the X-ray energy spectra shown in Fig. 9 as the ray source, and the emission position of the particle source was at the exit of the X-ray emission source (refer to Fig. 4). Figure 11 shows the X-ray energy spectra excited by different ores and received by the SDD for different values of d_{sea}. Figure 12 shows the characteristic X-rays corresponding to the four ores plotted as a trend with respect to d_{sea}. Simultaneously, to distinguish the seawater's effect on X-ray scattering or energy attenuation, another Geant4 simulation was conducted with seawater in a vacuum environment, and the SDD-detected target element characteristic X-ray trends under different vacuum layer thicknesses were statistically analyzed (d_{vac}: distance between the transmitter outer tube and rock layer in a vacuum environment).

The results show that in the absence of seawater interference with X-rays, the SDD detection efficiency showed an increasing and then a decreasing trend with increasing d_{vac}. However, when d_{vac} increased, the X-ray reflection holes projected a larger area onto the ore surface (the angle becomes larger), resulting in more X-rays reaching the SDD through the X-ray reflection holes. However, when d_{vac} exceeded a certain threshold, even if the projected area increased, the particle flux through the X-ray reflecting aperture decreased slightly, resulting in a slight decrease in the number of particles that can be detected by the SDD. Similarly, when the entire device was in seawater, owing to the attenuation effect of seawater on the X-ray energy [39], the detection efficiency of SDD decreased with increasing d_{sea} for ores with characteristic peak energies below 10 keV. However, to detect ores with characteristic peak energies exceeding 10 keV, such as Sr-containing ores, when $d_{sea} < 2$ mm, the increase in the projection area of X-ray reflection holes had a greater impact on the detection efficiency of SDD compared with that of the X-ray scattering or energy attenuation caused by seawater. Thus, the detection efficiency of SDD improves. When $d_{sea}>$

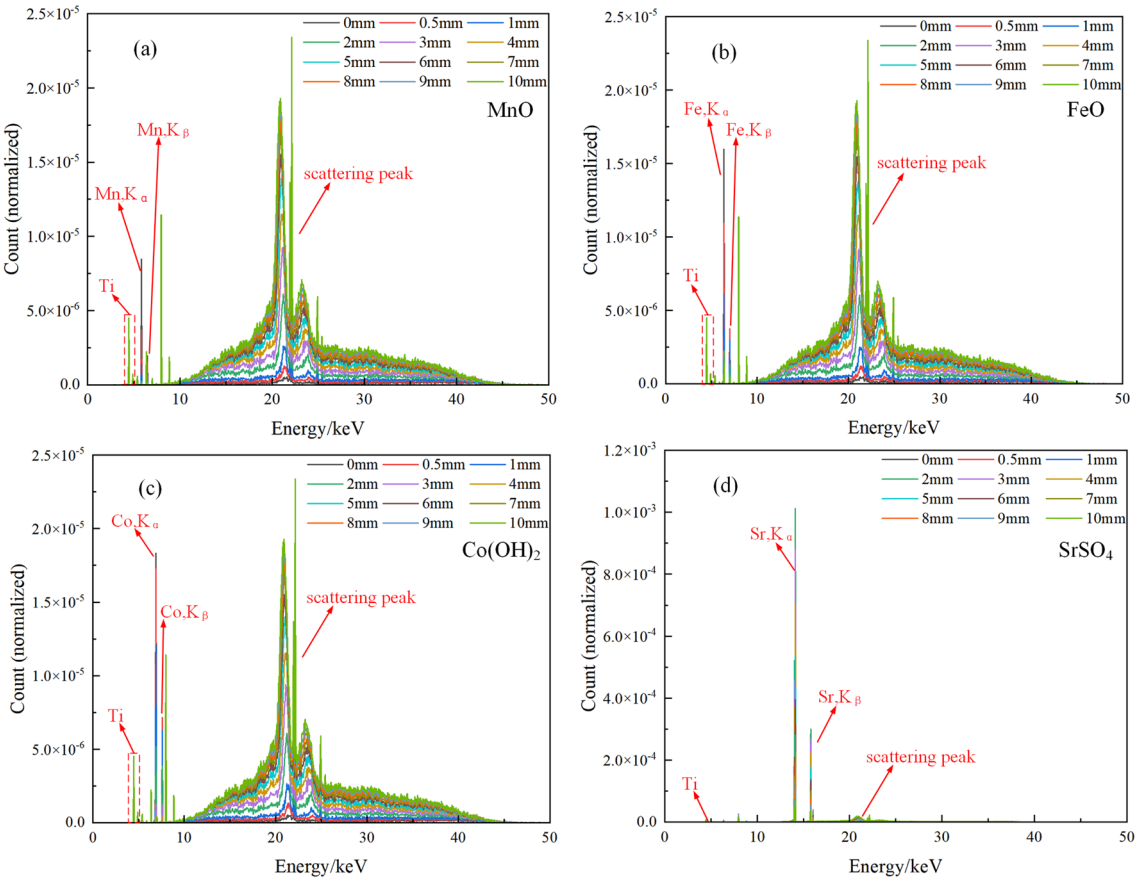

Fig. 11 (Color online) Different seawater thickness X-ray energy spectra of different ores received by SDD. **a** MnO X-ray energy spectra; **b** FeO X-ray energy spectra; **c** $Co(OH)_2$ X-ray energy spectra; **d** $Sr(SO)_4$ X-ray energy spectra

2 mm, the X-ray scattering or energy attenuation by seawater is the main influencing factor, and the detection efficiency of SDD decreases.

4 Conclusion

This paper presented the design of an X-ray probe tube for application in extreme environments such as the deep-sea. This study focused on the structural design, mechanical structure safety analysis, and detection efficiency optimization of target elements. The main results are as follows:

1. In a deep-ocean environment, an extreme working environment leads to deformation of the detector, which adversely affects its safety. Combining FEA and actual high-pressure and high-voltage damage test results, the Be window thickness can be selected at the appropriate ocean depth for exploration (For 3000 m seawater depth, d_{Be} = 1.5 mm; for 4000 m seawater depth, d_{Be} = 2.0 mm) to ensure the safety of the equipment.

2. From the Monte Carlo simulation experiments, it was observed that the size of d_{sea} should be appropriately adjusted according to the ore type. For ores with characteristic peak energies less than 10 keV, d_{sea} should be minimized during exploration. However, when the ore's characteristic peak energy is greater than 10 keV, d_{sea} should be increased to approximately 2 mm.

Note that the structural stability and corrosion resistance of the entire device in deep-sea under long-term working conditions may affect the detection efficiency of the detector. In addition, the analysis of the impact of the water content on the data will be investigated in subsequent experiments.

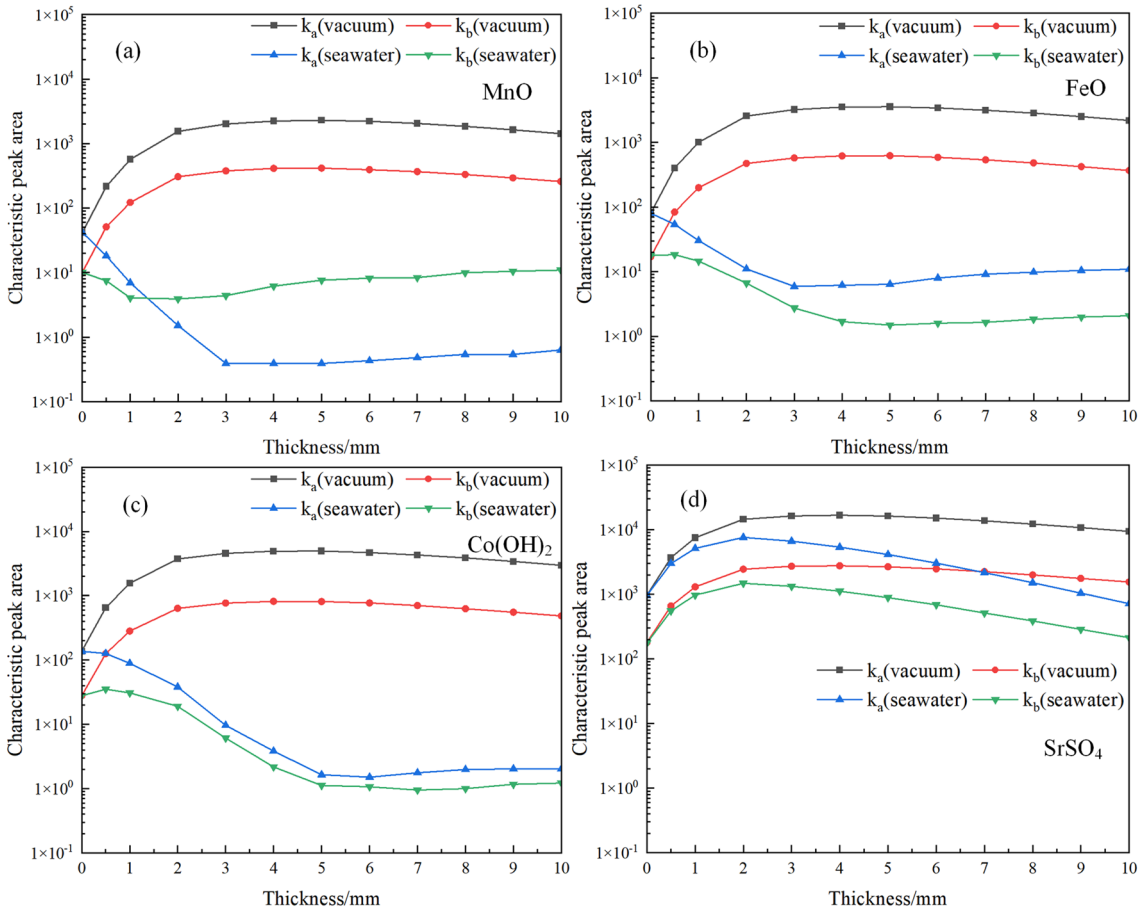

Fig. 12 (Color online) Trend plot of characteristic X-ray peak areas of different ores detected by SDD under different d_{sea} and d_{vac} conditions. **a** MnO characteristic X-ray peak area trend plot; **b** FeO characteristic X-ray peak area trend plot; **c** $Co(OH)_2$ characteristic X-ray peak area trend plot; **d** $Sr(SO)_4$ characteristic X-ray peak area trend plot

Author contributions All authors contributed to the study conception and design. Material preparation, data collection and analysis were performed by Lang Dong, Ming Wang and Qing-Xian Zhang. The first draft of the manuscript was written by Lang Dong and all authors commented on previous versions of the manuscript. All authors read and approved the final manuscript.

Data availability The data that support the findings of this study are openly available in Science Data Bank at https://cstr.cn/31253.11.sciencedb.j00186.00560 and https://doi.org/10.57760/sciencedb.j00186.00560.

Declarations

Conflict of interest The authors declare that they have no competing interest.

References

1. L.D. Meinert, G.R. Robinson, N.T. Nassar, Mineral resources: Reserves, peak production and the future. Resources **5**(1), 14 (2016). https://doi.org/10.3390/resources5010014
2. S. Rahul, Deep-sea mining: economic, technical, technological, and environmental considerations for sustain. Dev. Mar. Technol. Soc. J. **45**(5), 28–41 (2011). https://doi.org/10.4031/MTSJ.45.5.2
3. T. Prior, D. Giurco, G. Mudd et al., Resource depletion, peak minerals and the implications for sustainable resource management. Glob. Environm. Ch. **22**(3), 577–587 (2012). https://doi.org/10.1016/j.gloenvcha.2011.08.009
4. J.R. Hein, K. Mizell, A. Koschinsky et al., Deep-ocean mineral deposits as a source of critical metals for high- and green-technology applications: Comparison with land-based resources. Ore Geol. Rev. **51**, 1–14 (2013). https://doi.org/10.1016/j.oregeorev.2012.12.001
5. F. Sakellariadou, F.J. Gonzalez, J.R. Hein et al., Seabed mining and blue growth: exploring the potential of marine mineral deposits as a sustainable source of rare earth elements (MaREEs) (IUPAC Technical Report). Pure Appl. Chem. **94**(3), 329–351 (2022). https://doi.org/10.1515/pac-2021-0325
6. J.K. Yu, W.X. Cui, Explore China's stakeholders in the exploration and exploitation of mineral resources in deep seabed areas: Identification, challenges and prospects. Ocea. Coast. Manage. **244**(1), 106712 (2023). https://doi.org/10.1016/j.ocecoaman.2023.106712

7. L. A. Levin1, B.J. Bett, A.R. Gates et al., Global observing needs in the deep ocean. Front. Mari. Sci. **6**, 241 (2019). https://doi.org/10.3389/fmars.2019.00241
8. C. Schofield, Global Commons and the Law of the Sea, ed. by C. Schofield (Brill | Nijhoff, Leiden, Netherlands, 2018), pp. 151–167
9. X.L. Ju, B. Deng, K. Li et al., Calibrating the linearity between grayscale and element content for X-ray KES imaging of alloys. Nucl. Sci. Tech. **33**, 1 (2022). https://doi.org/10.1007/s41365-022-00986-3
10. B. Yang, Y.Y. Liu, J.W. Liao, Manned submersibles–deep-sea scientific research and exploitation of Marine resources. Bulletin of Chinese Academy of Sciences **36**(5), 622–631 (2021). https://doi.org/10.16418/j.issn.1000-3045.20210408004
11. R. He, X.Y. Niu, Yi Wang et al., Advances in nuclear detection and readout techniques. Nucl. Sci. Tech. **34**, 205 (2023). https://doi.org/10.1007/s41365-023-01359-0
12. C. Hauton, A. Brown, S. Thatje et al., Identifying toxic impacts of metals potentially released during deep-sea mining-A synthesis of the challenges to quantifying risk. Front. Mar. Sci. **4**, 368 (2017). https://doi.org/10.3389/fmars.2017.00368
13. L.A. Levina, K. Mengerinkb, K.M. Gjerdec et al., Defining "serious harm'' to the marine environment in the context of deep-seabed mining. Mar. Policy. **74**, 245–259 (2016). https://doi.org/10.1016/j.marpol.2016.09.032
14. P. Qiao, S.Q. Xiong, L.Q. Ge et al., Rock mineralogical characteristics and in-situ leaching uranium process test of Manglai uranium deposit in Erlian basin. Inner Mongolia. Miner. Petrol. **44**, 109–120 (2024).51.1143.TD.20240229.1354.002
15. Y.P. Kolmogorov, N.A. Mezentsev, A.G. Mironov et al., Development of a complex of instrumental nuclear–physical methods to detect PGE, Re, Au, and Ag in hard-to-analyze rocks and complex ores. Nucl. Instrum. Meth. Phys. Res. Sect. A **603**(1-2), 131–133 (2009). https://doi.org/10.1016/j.nima.2008.12.117
16. R. Sharma (ed.), *Perspectives on Deep-Sea Mining* (Springer Cham, India, 2022)
17. Z.H. Liu, K. Liu, X.G. Chen et al., Deep-sea Rock Mech. and mining technology: State of the art and perspectives. Inter. J. Min. Sci. Technol. **33**(9), 1083–1115 (2023). https://doi.org/10.1016/j.ijmst.2023.07.007
18. A. Hallgren, A. Hansson, Conflicting narratives of deep sea mining. Sustainability **13**(9), 5261 (2021). https://doi.org/10.3390/su13095261
19. R. Mukhopadhyaya, S.D. Iyerb, A.K. Ghoshc, The Indian Ocean Nodule Field: petrotectonic evolution and ferromanganese deposits. Earth-Sci. Rev. **60**(1–2), 67–130 (2003). https://doi.org/10.1016/S0012-8252(02)00078-8
20. N. Toro, R.I. Jeldres, J.A. Órdenes et al., Manganese nodules in chile, an alternative for the production of Co and Mn in the future-A review. Minerals **10**(8), 674 (2020). https://doi.org/10.3390/min10080674
21. H.W. Yu, Y.X. Zhang, X.H. Chen et al., Numerical simulation and method study of X-ray litho-density logging. Nucl. Sci. Tech. **31**, 124 (2020). https://doi.org/10.1007/s41365-020-00826-2
22. Y. Dai, X.Y Li, W.W. Yin et al., Dynamics analysis of deep-sea mining pipeline system considering both internal and external flow. Mari. Geores. Geotechnol. **39**(4), 408–418 (2019). https://doi.org/10.1080/1064119X.2019.1708517
23. W. Chen, H.L. Xu, N. Peng et al., Linkage characteristics of deep-sea mining lifting system. Ocean Eng. **233**, 109074 (2021). https://doi.org/10.1016/j.oceaneng.2021.109074
24. S.J. Zhang, *Dissertation (Jiangsu University of Sci* (Mech. Eng, Technology, 2018)
25. X. Huang, Dissertation, Qingdao University of Science & Technology, Power Eng. and Engineering Thermophysics, 2018 (in Chinese)
26. R.N. Elshaer, K.M. Ibrahim, Study of microstructure, mechanical properties, and corrosion behavior of As-cast Ni-Ti and Ti-6Al-4V alloys. J. Mater. Eng. Perform. **32**, 7831–7845 (2023). https://doi.org/10.1007/s11665-022-07654-y
27. Los Alamos National Laboratory. Beryllium Oxide (BeO) Handbook, https://www.osti.gov/biblio/1635499; 2020[accessed 1 May 2020]
28. T. Kakiuchi, R. Kawaguchi, M. Nakajima et al., Prediction of fatigue limit in additively manufactured Ti-6Al-4V alloy at elevated temperature. Int. J. Fatigue. **126**, 55–61 (2019). https://doi.org/10.1016/j.ijfatigue.2019.04.025
29. J. Ding, R. Hall, J. Byrne, Effects of stress ratio and temperature on fatigue crack growth in a Ti-6Al-4V alloy. Int. J. Fatigue. **27**, 1151–1558 (2005). https://doi.org/10.1016/j.ijfatigue.2005.06.007
30. Y. Gu, S.Q. Xiong, L.Q. GE et al., Research on spectral characteristic of miniature X-ray tube and determination of beryllium window thickness. Spectrosc. Spect. Anal. **34**(1), 252–256 (2014). https://doi.org/10.3964/j.issn.1000-0593(2014)01-0252-05
31. Y. Lu, N. Huang, The filter effects in X-ray tube XRF simulated by using the MCNP5 code. Nucl. Tech. (in Chinese) **35**(10), 751–754 (2012)
32. A. Ji, Development of X-ray fluorescence spectrometry in the 30 Years. Rock and Mineral Analysis **31**(3), 383–398 (2012). (**in Chinese**)
33. S.L. Liao, C.H. Tao, H.M. Li et al., Use of portable X-ray fluorescence in the analysis of surficial sediments in the exploration of hydrothermal vents on the Southwest Indian Ridge. Acta Oceanol. Sin. **36**, 66–76 (2017). https://doi.org/10.1007/s13131-017-1085-0
34. B. Buyuk, Preparation and characterization of iron-ore-imbedded silicone rubber materials for radiation protection. Nucl. Sci. Tech. **29**, 135 (2018). https://doi.org/10.1007/s41365-018-0459-0
35. B.G. Lowe, R.A. Sareen, *Semiconductor X-Ray Detectors* (CRC Press, Boca Raton, 2014)
36. M. Bass, Handbook of Optics: Volume II - Design, Fabrication, and Testing; Sources and Detectors; Radiometry and Photometry, 3rd edn. (McGraw-Hill, New York, 2010)
37. C.D. Mobley, *Light and Water: Radiative Transfer in Natural Waters' Academic Press* (Academic Press, California, 1994)
38. G.L. Liou, A.M. Barnett, Prototype GaAs X-ray detector and preamplifier electronics for a deep seabed mineral XRF spectrometer. X-Ray Spectrom. **47**(3), 201–214 (2018). https://doi.org/10.1002/xrs.281
39. R. Bagheri, A.K. Moghaddam, B. Azadbakht et al., Determination of water equivalent ratio for some dosimetric materials in proton therapy using MNCPX simulation tool. Nucl. Sci. Tech. **30**, 31 (2019). https://doi.org/10.1007/s41365-019-0544-z

Springer Nature or its licensor (e.g. a society or other partner) holds exclusive rights to this article under a publishing agreement with the author(s) or other rightsholder(s); author self-archiving of the accepted manuscript version of this article is solely governed by the terms of such publishing agreement and applicable law.